ELSEVIER

Journal of Structural Geology 28 (2006) 1767–1784

JOURNAL OF STRUCTURAL GEOLOGY

www.elsevier.com/locate/jsg

Shallow crustal fault rocks from the Black Mountain detachments, Death Valley, CA

Nicholas W. Hayman*

Division of Earth and Ocean Sciences, Box 90227, 103 Old Chemistry Building, Duke University, Durham, NC 27708, USA

Received 10 February 2006; received in revised form 3 June 2006; accepted 30 June 2006
Available online 6 September 2006

Abstract

The Black Mountain detachments denuded crystalline footwalls and extended sedimentary hanging walls from late Pliocene to Recent time. Fault rocks include gouges that crosscut breccias, and are in turn cut by compositionally and texturally distinct shear bands. Breccias have cataclastic textures, noteworthy for abundant transgranular fracture and power-law particle size distributions (D) of 2.77–2.79. Gouges have granular textures, noteworthy for grains with abraded boundaries surrounded by a clay-rich matrix and $D = 2.86–3.31$. Matrix minerals include phyllosilicates, clay minerals, and oxide aggregates that serve as crude strain indicators. Geochemical data indicate that there was abundant water within the fault zone, but that the water was not plumbed from deeper crustal sources. There are systematic geochemical variations between fault-rock samples, but the inferred mass changes were minor, $<10–30\%$. It is proposed that the fault rocks developed during exhumation since the late Pliocene from ≥ 3 km to near-surface conditions. Exhumation coincided with the development of granular textures and strain localization. The protracted history of the fault rocks involved multiple deformation mechanisms and authigenic mineral assemblages that hypothetically influenced the frictional properties of the detachment shear zones.

Keywords: Fault rock; Gouge; Cataclasite; Detachment; Low-angle normal fault

1. Introduction

There is a long-standing hypothesis that fault rocks play an important role in the strength, seismicity, and permeability of fault zones (Sibson, 1977). Experiments and theory have found numerous ways that the frictional strength and stability of faults depends on mineralogy, texture, and the state of stress (Byerlee, 1978; Rice, 1992; Marone, 1998; Faulkner and Rutter, 2001; Mair et al., 2002). Motivated by mechanical hypotheses, many workers have studied natural fault zones only to find difficult-to-interpret structural and geochemical patterns (Chester and Logan, 1987; Evans and Chester, 1995; Manatschal et al., 2000; Yonkee et al., 2003). Studies of natural fault rocks are therefore an ongoing effort that requires careful assessment of multiple, diverse fault localities.

Important fault-rock localities are shallowly dipping ($\leq 30°$) detachment shear zones that bound the west-northwest flanks of the Black Mountains, Death Valley, CA (Miller, 1996; Cowan et al., 2003). The detachments belong to a class of faults that are controversial in part because their shallow dip requires that they were weak relative to more steeply dipping faults and laboratory values for rock friction (Axen, 2004). Previous studies showed how distributed deformation of the fault rocks accommodated large shear strains (Cladouhos, 1999a,b; Cowan et al., 2003; Hayman et al., 2004). Yet, without a more complete understanding of the time-depth history of the fault rocks, and the range of chemical and deformational processes that operated within them, the mechanics of the detachments will remain uncertain.

New data presented here lead to a conceptual model wherein the fault rocks developed during tectonic denudation

* Tel.: +1 919 681 8165.
E-mail address: hayman@duke.edu

0191-8141/$ - see front matter © 2006 Elsevier Ltd. All rights reserved.
doi:10.1016/j.jsg.2006.06.017

of ~3 km of sedimentary cover from the Black Mountain crystalline core since the late Pliocene. Reconstructing this protracted history finds that different grain-scale, brittle-frictional, deformation mechanisms dominated at different times. Water-rock reactions, though significant, left a narrow range of alteration minerals and systematic compositional variations. The presentation of the conceptual model requires weaving together a variety of structural, mineralogical, and geochemical arguments. The data and interpretations in turn contribute to our understanding of fault mechanics, inspiring a brief discussion of mechanisms for both static and dynamic weakening of fault zones.

2. The Black Mountain detachments

The Black Mountain detachments bound the east side of Death Valley, CA, and are an archetypical result of basin-and-range extension and concomitant exhumation of middle crustal rocks (Wright et al., 1974; Asmerom et al., 1990). In order to understand the detachments that flank the Black Mountains, gneisses and the shallow-crustal fault rocks, an overview of the footwalls, hanging walls, and detachment shear zones is presented here.

2.1. The footwalls

The Black Mountain detachments define the upper surface of the Mormon Point, Copper Canyon, and Badwater *turtlebacks* (Wright et al., 1974), analogous to the cores of metamorphic core complexes (Lister and Davis, 1989) (Fig. 1). The rocks that form the footwall of most detachment localities are late Proterozoic carbonate and siliceous gneisses and early Proterozoic quartzofeldspathic basement (Drewes, 1963; Wright and Troxel, 1984; Miller, 1992). Pegmatitic and basaltic dikes and sills intrude the Proterozoic rocks, along with larger bodies such as the Miocene-age Willow Springs diorite and the Smith Mountain granite (Asmerom et al., 1990; Wright et al., 1991). Thus, footwall-derived clasts, or *survivor grains* (cf. Engelder, 1974), within the detachment shear zones will have carbonate and/or quartzofeldspathic lithologies, and will be distinctive for either an internal mylonitic fabric or magmatic textures.

The crystalline rocks in the turtlebacks have long deformation histories, culminating in penetrative crystal plastic and semibrittle deformation that was roughly coeval with the emplacement of the Miocene intrusive bodies (Wright et al., 1991; Miller, 1992). All three turtlebacks were brought to upper crustal depths from 10 to 6 Ma (Holm and Dokka, 1993). Mylonitic and semibrittle deformation accommodated much of this uplift, but late Miocene-early Pliocene basaltic dikes and flows (Holm et al., 1994) crosscut the resulting foliation (Hayman, 2003). The detachments strike and dip at a low angle to, and crosscut, pre-to-early Miocene foliations and structures and younger intrusive rocks (Wright et al., 1991; Hayman, 2003). Thus, a continuous transition from crystal plastic to semibrittle to brittle-frictional structures probably did not occur in the Black Mountain detachments.

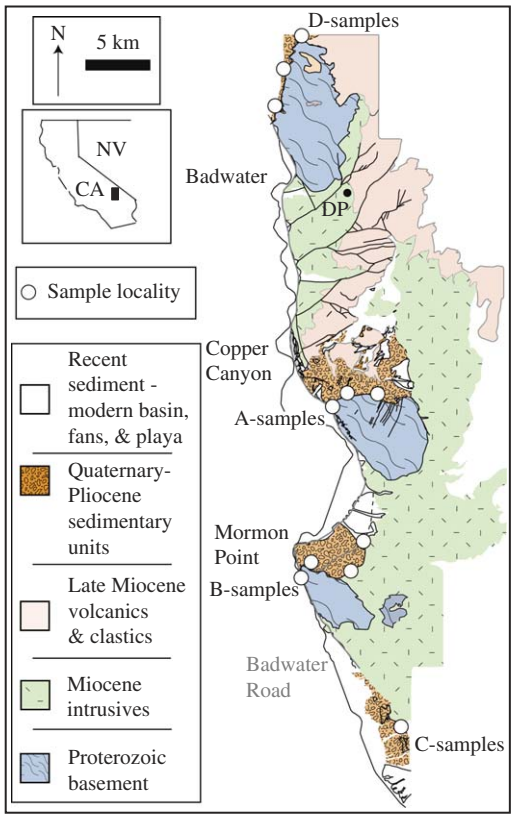

Fig. 1. Geologic map of the Black Mountains, Death Valley, California (see inset for geographic location relative to the Nevada (NV)-California (CA) border). Compiled from Drewes (1963), Wright and Troxel (1984), and Miller (1992). Dante's Peak (DP) is at 1669 m and the deepest elevation in Death Valley, west of Badwater, is −86 m, below sea level. High-angle faults are thin lines and the low-angle normal, detachment faults are bold lines. Sample locations are white circles.

2.2. The hanging walls

The Copper Canyon detachment demonstrably cuts the Pliocene (ca. 3.1 Ma) Copper Canyon formation (Holm et al., 1994), and all of the detachments cut correlative-to-younger late Pliocene (ca. 1.2 Ma) Funeral formation. The detachments cut well-dated Pleistocene-age (ca. 0.76 Ma) Mormon Point formation and kinematically linked, higher angle faults cut younger Pleistocene through Quaternary (ca. 0.76–0.1 Ma) volcaniclastic, lacustrine, and aluvial deposits (Knott et al., 1999). Although growth-strata relationships are not clearly defined, there is evidence that the detachments have generally been active throughout the depositional history (Holm et al., 1994; Knott et al., 1999; Hayman, 2003; Hayman et al., 2003).

The clasts of the hanging wall are dominated by some combination of reworked volcaniclastics, tephra, basalt, and Proterozoic basement. Clasts from Late Proterozoic gneisses and Miocene intrusives are less abundant except in the youngest gravels. Therefore, it is generally possible to differentiate between hanging-wall derived lithic fragments and footwall-derived clasts.

During some intervals of detachment slip, the hanging walls were internally extended by high-angle faults that

sole into the detachments. At other times the detachments translated the hanging walls without internal faulting, denuding the footwall. Thus, the frictional strength of the detachments relative to the hanging walls changed over time, and was weak ($\mu < 0.4$) during some slip intervals (Hayman et al., 2003). Lastly, some increments of hanging-wall faulting produced earthquake scarps, demonstrating that the detachments were seismogenic at times, or at least did not dampen propagating seismic rupture (Hayman et al., 2003).

2.3. The detachment shear zones

The Black Mountain detachments differ from the widely reported fault-structure of a high strain fault core symmetrically surrounded by a lower strain damage zone (cf. Chester and Logan, 1987). Rather, strain is asymmetrically distributed, increasing upward from the footwall into foliated breccia units, into gouge units (Cowan et al., 2003). Though damage zones are not an integral part of every detachment locality, there are damage zones in the detachment footwalls near segment ends and intersections (Fig. 2a) (Pavlis et al., 1993).

The *foliated breccia* (Fig. 2b) is distinctive for compositional banding and lenticular survivor grains. Greater than 90% of survivor grains are footwall-derived (Hayman et al., 2004) although there are localities where mesoscopic lenses of hanging-wall sediment were incorporated into the foliated breccia (Cowan et al., 2003). The contact between the foliated breccias and footwall is in many places gradational and microfaults, fractures, and veins can be found to extend from the footwall into the shear zones (Fig. 2b).

Gouge typically overlies and cuts the foliated breccia (Figs. 2b and 3a) and can be subdivided into *granular*, *clay*, *or scaly clay gouge* (Fig. 3c,d) (Cladouhos, 1999a,b). There are foliated and unfoliated gouges, and most have a distinctive banding of carbonate and/or quartzofeldspathic lithologies surrounded by matrix minerals (Fig. 3b) (Miller, 1996; Cowan et al., 2003). In many gouges the survivor grains have abraded grain-boundaries and smaller clasts are strewn throughout the surrounding fine- to clay-sized matrix (Fig. 3c).

Shear bands cut the gouge and breccia units. These centimeter-to-millimeter-wide planar and curviplanar structures include the principal slip plane at the top of the shear zone, and other Y-, P- and R-oriented bands (terminology of Chester and Logan, 1987; Cladouhos, 1999a,b; Cowan et al., 2003). The shear bands crosscut or define some fault-rock unit boundaries and crosscut most surrounding structures and foliations (Fig. 3c). It has been suggested that the shear bands are the expression of localization of an asymmetric finite-strain gradient across the shear zones (Cowan et al., 2003), or that they are kinematic necessities throughout the strain history (Cladouhos, 1999a,b). These slightly contradictory hypotheses

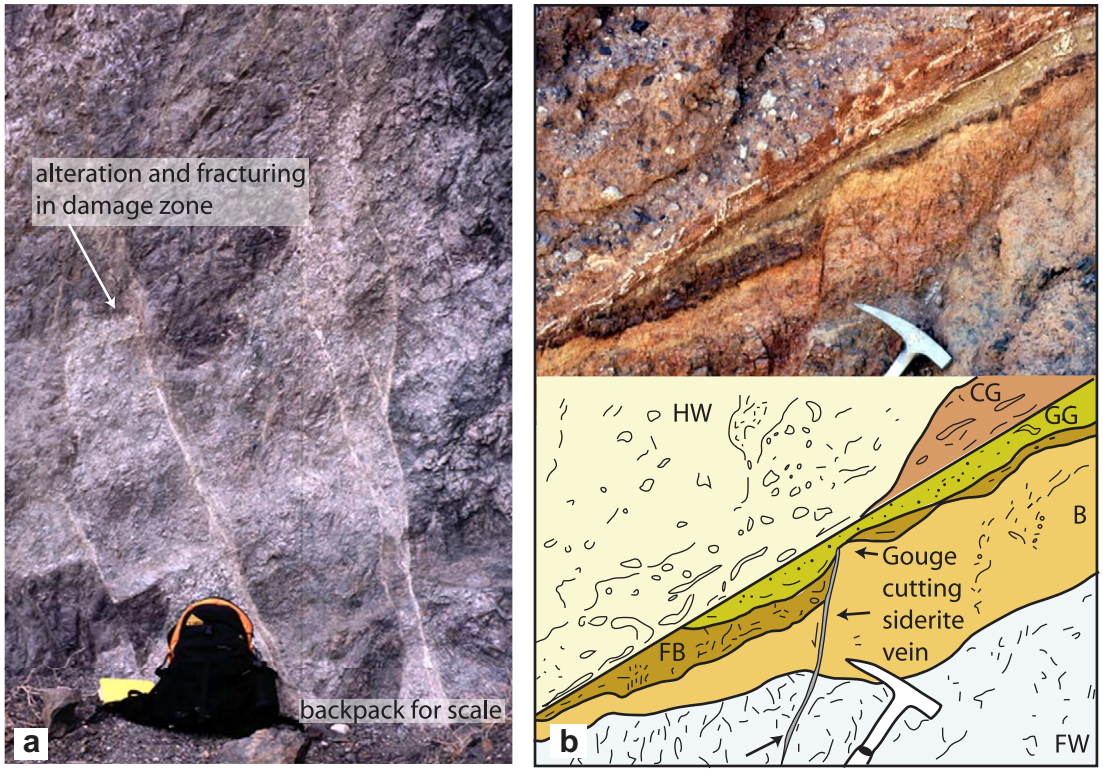

Fig. 2. Damage-Zone structures: (a) Damage zone structurally below the Copper Canyon detachment; Note the "bleaching" effect from damage-zone related alteration; (b) Photograph and sketch of the Badwater detachment. HW = Hanging Wall, CG = Clay Gouge, GG = Granular Gouge, FB = Foliated Breccia, B = Breccia (undifferentiated), FW = Footwall (abbreviations the same throughout the text). Crosscutting relationships indicate that mineralization such as siderite veining and damage-zone related fracturing continued after the initial development of the foliated breccia, but predates the gouge deformation.

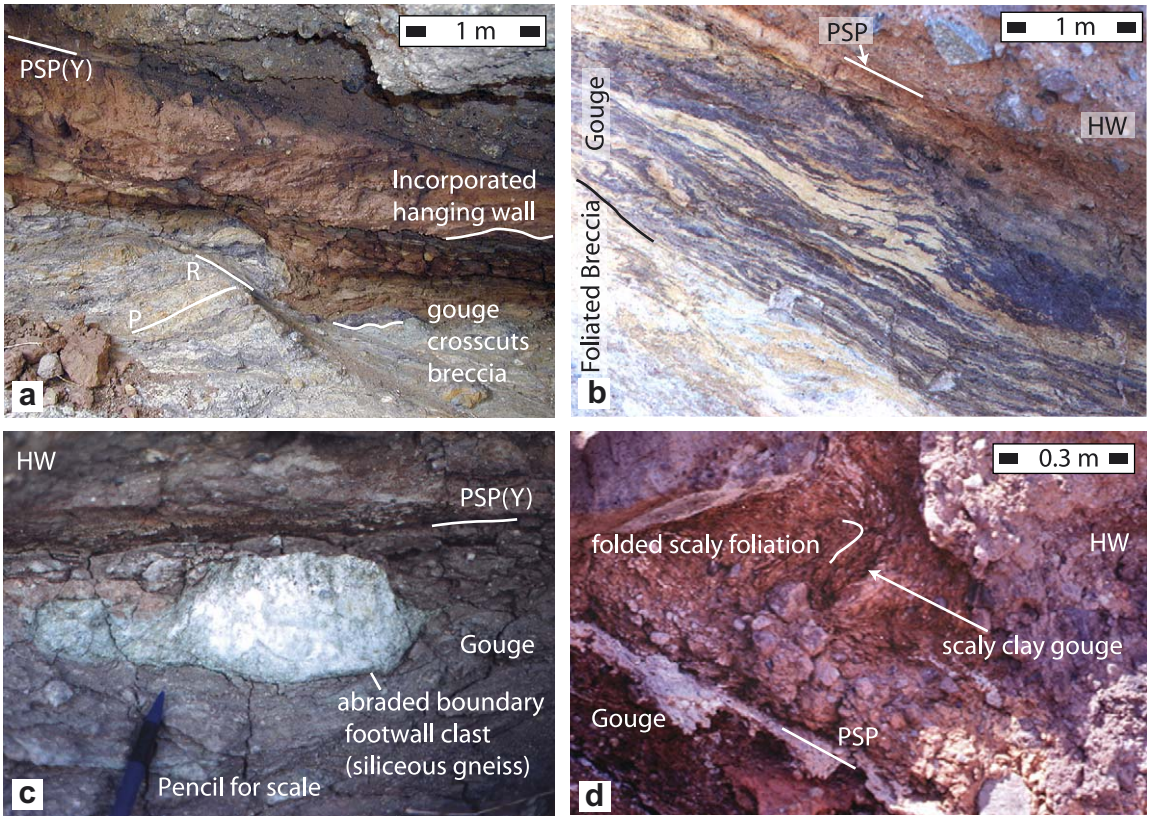

Fig. 3. Detachment fault-rock structure: (a) exposure of a detachment segment south of Mormon Point, colloquially referred to as the ''Size 36'' detachment. Gouge crosscuts the P- and R-fabrics in the foliated breccia. The light brown body in the gouge unit, below the principal slip plane (PSP), is a meter-scale lens of hanging-wall sediment (Photograph courtesy of Julia Morgan). (b) Asymmetric zonation of fault rocks across the Badwater detachment and ptygmatic folds in compositional bands in gouge. PSP = Principal Slip Plane. (c) A clast of siliceous gneiss suspended within clay gouge in the Mormon Point detachment. The clast's grain boundaries are abraded, and small clasts of the gneiss are disseminated throughout the gouge. (d) Scaly clay gouge from the Badwater detachment located above the principal slip surface which elsewhere separates hanging-wall sediment from clay gouge.

contrast with those from other localities where shear bands are proposed to have accommodated most of the (coseismic) strain history (Chester and Chester, 1998).

3. Methods

3.1. Overview and sample preparation

Samples were collected at several localities along the detachment exposures and at several vertical positions across the shear zones (Fig. 1) (see also Cowan et al., 2003). Analytical techniques used to study the fault rocks include: optical microscopy, scanning electron microscopy (SEM), transmitted electron microscopy (TEM), X-ray diffraction (XRD), X-ray fluorescence (XRF), laser particle size analysis (LPSA) determinations of particle size distributions (PSD), and determination of oxygen isotope compositions (Tables 1–4). Exxon Production Research Company (now Exxon-Mobil Technology Company) commercially attained or directly provided much of the PSD, XRD, XRF, and all of the oxygen isotope data. Each analytical technique required a different preparation technique that either benefited or was hindered by the incohesive character of the fault rocks; most of the fault rocks crumble easily, and disaggregate readily in water.

For optical microscopy and SEM, samples were impregnated with a low viscosity epoxy under vacuum at 60 °C. The resulting billets were then trimmed and polished dry, and mounted for final thin section preparation including a diamond-grit polish. Transmission Electron Microscopy (TEM) grids were prepared by cutting ~1 cm-diameter wafers from thin sections prepared with alcohol-soluble epoxy. The wafers were then mounted on a copper grid and thinned with an ion mill.

Sample preparation for all other analyses began by immersing the sample in deionized water and 0.5% $(NaPO_3)_6$ (Calgon) as a dispersant, and then placing the solution in an ultra-sonic cleanser for 2 min. Disaggregating some samples required ~30 s of direct impact with a mortar and pestle. For X-ray diffraction (XRD) the disaggregated sample was wet-sieved with a 63-μm mesh and <2 μm separates were prepared with a centrifuge (assuming stokes settling) and mounted using a Millipore filter (see Moore and Reynolds, 1997). Exxon-Mobil Technology Company dispersed samples with a freeze-thaw method.

3.2. Analyses

SEM was conducted in backscattered electron (BSE) mode on the JEOL 730 superprobe at the University of Washington.

Table 1
PSDs calculated by laser particle size analyzer (<63 μm), and sieving and weighing (>63 μm)

Sample	Type	Position	*D*	<62.5 μm	<31.3 μm	<11 μm	<3.9 μm	<2 μm
A21	HW	0.2	2.45	8.53	6.84	4.61	2.54	1.38
A7	HW	0.1	2.52	10.02	8.49	5.87	3.08	1.96
B10	FW	−7	2.43	7.12	5.58	3.58	1.72	0.76
C4	FW	−1	2.63	16.65	13.44	8.48	3.92	1.85
A53	FW	−1	2.79	33.5	25.6	15.5	7.3	3.1
A27	FB	−0.1	2.77	26.7	19.7	11.2	4.4	1.7
A26	GG	−0.15	2.87	35.2	29.5	21.8	12.2	5.9
C3	GG	−0.2	2.87	37.58	32.22	24.72	15.64	8.47
B6	GG	−0.3	3.03	48.9	44.23	36.05	24.31	14.23
D3	G	−0.3	2.86	40.8	35.1	24.8	12.9	6.2
A45	G	−0.35	2.86	38.8	31.9	21.5	10.8	4.7
B2	G	−0.3	2.99	55.3	47.8	35.7	21.1	11.4
D26	G	−0.6	3	58	48.2	36.2	24.7	15.6
A25	G	−0.4	3.09	99.5	99.5	99.5	87.1	62
B7	G	−0.4	3.13	50.51	46.67	39.1	27.36	16.8
D2	G	−0.1	3.19	99.9	99.9	84.2	54.4	32.1
D11	CG	−0.1	3.14	67.23	60.21	48.32	30.81	17.19
B1	CG	−0.2	3.19	100	100	85.9	54.9	30.1
A47	CG	0	3.31	99.7	99.7	86.1	58.6	33.9
A23	SCG	−0.05	3.06	69.1	58.1	42.5	27.5	16.4

G = undifferentiated gouge. Position is the vertical distance from the principal slip plane with "−" below the plane (convention is the same for all tables). *D* is the dimensionless power-law slope displayed in Fig. 8. Other columns are "weight % less than". Fig. 8 displays some representative PSD spectra.

Minerals were identified with electron dispersive spectroscopy (EDS) including the construction of element maps. TEM images were produced on a Philips CM300FEG, 300-kV, field-emission gun electron microscope at the Johns Hopkins University. Mineralogy and compositions of grains imaged with TEM were determined by electron diffraction and X-ray emission spectroscopy (qualitatively equivalent to EDS).

XRD analyses (Table 2) were attained with Cu K-α radiation at 40 mA and 50 kV. Scans proceeded at 0.01°2θ/s. Identification of mixed-layer clays used the program NEWMOD (Moore and Reynolds, 1997).

XRF analyses (Table 3) were commercially attained from XRAL. The XRF technique has precision and accuracy typically well under 1% 2σ with the possible exception of Na and P; note that totals for all analyses range from 97.82–100.2 wt.%.

Oxygen isotope compositions (Table 4) were commercially attained by Exxon-Mobil Production Research, and determined for powders of three different size fractions, <0.02 μm, <0.2 μm, and <2 μm (by centrifuge, assuming Stokes settling). The compositions were reported as:

$$\delta^{18}\mathrm{O} = \frac{(^{18}\mathrm{O}/^{16}\mathrm{O})_{\mathrm{sample}} - (^{18}\mathrm{O}/^{16}\mathrm{O})_{\mathrm{SMOW}}}{(^{18}\mathrm{O}/^{16}\mathrm{O})_{\mathrm{SMOW}}}$$

with a precision of 0.1 per mil.

PSD data (Table 1) were attained with a 120-detector laser particle size analyzer (LPSA). PSDs are reported as both the weight percent of specific size fractions, and as the power-law slope (*D*) determined by plotting the log of the cumulative number (*N*) against the log of the size (*S*): $N(S) = S^{-D}$ (Sammis et al., 1987). The >63 μm fraction was sieved and weighed because the LPSA resolution has an upper limit between 100 μm and 1 mm. In fact, the upper limit of resolution is more a matter of the number of particles in any volume than an instrumental consideration. For example, samples with virtually no particles >63 μm (e.g., sample A47) have a power-law slope defined by the size fraction between ~2–63 μm. Extensive calibration can produce LPSA data <1 μm (Sperazza et al., 2004; Wilson et al., 2005), but generally LPSA data are unreliable at such grain sizes. LPSA instrument software determines PSD by modeling the collective volume with diffraction theory and assumes Stoke's law. For particles <2 μm the breakdown of the spherical-particle assumption and flocculation can affect the PSD. Furthermore, sample preparation can introduce an excess of fine particles thereby artificially increasing *D*-values. Altogether, the precisions of power-law slopes are at best ±0.1 (Vrolijk et al., 1997).

4. Microstructures

At the thin-section scale, the diagnostic character of the fault rocks is the *clast-in-matrix* texture wherein clasts, or survivor grains, are surrounded by a matrix of comminuted material and secondary minerals. The clast-in-matrix texture can be further subdivided into *cataclastic* and *granular* textures (cf. Twiss and Moore, 1992). Cataclastic textures, found primarily in the breccias, are distinctive for contacts between clasts, and transgranular fractures that cross grain boundaries or radiate from grain contacts (Fig. 4a). Granular textures, found mostly in the gouges, are distinctive for clasts that are separated by a finer grained matrix and, where present, have transgranular fractures that do not cross grain boundaries (i.e. predate gouge deformation) (Fig. 4b). Some gouges, and granular gouges in particular, have compositional banding, here called *microbands* (Fig. 4b).

Table 2
XRD mineral identification

Type	Sample	Position	Ab	Or	Cte	Dol	Q	Hem	Chl	Musc	Sap	C-S	I-S	%Exp
Copper Canyon														
HW	A-7	0.1	X	X	X		X	X	X	X			X	NA
HW	A-13-2	0.1	X	X	X		X	X	X	X	X		X	80
SCG	A-10	−0.05	X	X	X	X	X		X			X		90
SCG	A-11	−0.1	X		X		X	X	X			X		40
SCG	A-23	0.05	X	X	X		X	X	X				X	70
CG	A-13-1	−0.1	X	X	X		X	X	X	X		X		50
CG	A-24	0	X		X	X	X	X			X			100
G	A-25	−0.4	X	X	X	X	X	X				X		50
G	A-45	−0.35	X	X		X		X			X			100
G	A-47	0	X	X	X		X	X	X				X	60
G	A-49	−0.4	X			X	X				X			100
GG	A-26	−0.15	X	X	X	X	X	X	X			X		45
FB	A-9	−0.2	X	X	X		X	X	X		X	X		50
FB	A-27	−0.1	X		X	X					X			100
FW	A-52	−0.5	X					X	X		X			100
FW	A-53	−1	X		X						X			100
FW	A-54	−2.5	X								X			100
FW	A-55	−4			X				X		X			100
FW	A-56	−15	X	X	X		X		X		X			70
Mormon Point														
CG	B-1a	−0.2	X	X		X	X			X			X	70
CG	B-1b	−0.2	X	X	X	X	X			X			X	70
GG	B-2	−0.3	X	X	X	X	X		X				X	70
G	B-7	−0.4	X	X	X		X	X	X				X	70
FW	B-8	−15	X	X	X		X		X				X	70
FW	B-10	−7	X	X			X	X	X				X	NA
Badwater Turtleback														
HW	D-22	0.06	X	X	X		X	X					X	50
PSP	D-14	0	X	X	X		X						X	70
CG	D-11	−0.1	X	X	X		X	X	X				X	NA
G	D-2	−0.1	X	X	X	X	X		X	X			X	NA
G	D-3	−0.3	X	X	X		X			X			X	NA
G	D-26	−0.5	X	X		X	X	X						NA
FB	D-18	−0.4	X	X	X		X		X				X	NA

Ab = albite, Or = orthoclaste, Cte = calcite, Dol = dolomite, Q = quartz, Hem = hematite, Chl = chlorite, Musc = muscovite, Sap = saponite, C-S = interstratified chlorite-saponite, I-S = interstratified illite-smectite, %Exp = percent expandable layers in interstratified clays. Additional manganese and iron oxides such as siderite, goethite, and limonite are present in the fault rocks, but were not resolved in XRD.

Clay and scaly clay gouges are more compositionally homogeneous and thoroughly mixed (Fig. 4c). Many clasts in the gouge have abraded grain boundaries (Fig. 4d).

In places, gouge contains large grains of high atomic weight (high contrast in BSE) surrounded by finer grained *halos* (Fig. 5a,b). X-ray mapping shows that the halos are manganese-rich, irregular alteration patterns around rhodochrosite in some places, and manganese oxide in others. In some samples the halos are flattened and stretched relative to their otherwise more irregular morphology. Interpreted as crude strain markers, asymmetric tails to the flattened halos indicate the maximum stretching direction of non-coaxial, finite shear strain.

TEM images of the clay gouge show the submicron character of the matrix. The matrix fabric is defined by finely packed phyllosilicates, and mostly clay minerals (Fig. 6a). The phyllosilicates have individually lath-like habits, but as aggregates ''wrap'' around clasts. Some of the phyllosilicates in the matrix are highly ordered with unstrained, evenly spaced {001}-lattice fringes. Other grains have interstratified phases with some (intracrystalline) strained lattice fringes between unstrained ones (Fig. 6b).

The shear bands are >1 cm to <1 mm wide and, at the microscale, contain comminuted material with no obvious internal fabric (Fig. 7) (but see Hayman et al., 2004). It is noteworthy in this context that fault rocks from other localities are reported to have undergone comminution via transgranular fracture down to micron-to-submicron grain sizes (Wilson et al., 2005; Chester et al., 2005). There is no evidence to date that transgranular fracture is a major component of the submicron texture of the Black Mountain granular-textured gouges, inspiring the interpretation that interparticle slip dominated gouge deformation. In contrast, the shear bands may represent a fundamentally different response to fault-slip than the surrounding granular textures.

5. Particle size distribution

The fault-rock microstructures described in Section 4 are quantified by the particle size distribution (PSD) (Fig. 8; and

Table 3
XRF of fault and wall rocks

Sample	Type	Position	$SiO_{2\%}$	$TiO_{2\%}$	$Al_2O_{3\%}$	$Fe_2O_{3\%}$	MnO%	MgO%	CaO%	Na_2O %	K_2O%	LOI%	Total
Copper Canyon													
A7	HW	0.1	63.0	0.517	13.10	3.33	0.11	1.01	4.84	3.79	4.68	3.90	98.28
A10	SCG	−0.05	42.9	0.657	9.88	12.00	0.08	9.56	10.90	0.48	2.15	11.10	100.0
A11	SCG	−0.1	42.4	0.989	13.40	9.13	0.12	10.60	7.18	1.74	2.38	11.60	99.54
A26	CG	−0.15	55.7	0.744	12.50	6.96	0.08	8.39	3.25	2.85	1.87	7.45	100.2
A49	G	−0.4	45.8	0.301	11.70	10.50	0.05	13.30	9.52	0.88	0.33	7.50	99.88
A55	FW	−4	37.9	0.584	13.30	5.91	0.04	16.70	12.60	0.75	2.57	8.50	98.85
A56	FW	−15	64.1	0.840	16.00	5.77	0.07	1.69	3.25	4.21	1.75	1.25	99.6
Mormon Point (graphically presented in Cowan et al., 2003*)*													
B1a	CG	−0.2	60.0	0.463	13.80	4.05	0.26	3.12	3.96	2.45	4.17	7.70	99.97
B1b	CG	−0.2	60.8	0.358	13.30	2.65	0.25	2.30	5.60	2.80	4.06	8.05	100.17
B1m			60.4	0.4	13.6	3.4	0.3	2.7	4.8	2.6	4.1	7.9	100.1
B1sd			0.6	0.1	0.4	1.0	0.0	0.6	1.2	0.2	0.1	0.2	0.1
B2	GG	−0.3	51.7	1.110	15.50	6.79	0.28	2.72	6.46	4.78	2.55	7.95	99.84
B8	FW	−15	64.3	0.682	16.00	4.78	0.06	3.12	0.53	4.01	3.96	2.05	99.49
Badwater													
D22	HW	0.06	70.2	0.229	13.00	3.32	<0.01	0.06	0.75	1.37	9.27	1.15	99.35
D14	PSP	0	19.3	0.193	5.91	2.77	0.44	3.91	34.50	0.67	2.44	30.10	100.23
D11	CG	−0.1	55.6	1.050	15.10	5.68	0.49	2.07	5.04	2.54	5.68	6.55	99.80
D2	G	−0.1	50.7	0.478	11.90	5.83	0.55	4.97	7.51	1.63	4.25	12.20	100.02
D3	G	−0.3	70.3	0.599	14.70	3.54	0.08	0.77	0.61	2.04	5.07	2.15	99.86
D18	FB	−0.4	62.1	0.488	14.50	4.93	0.08	2.77	3.67	3.25	3.91	4.30	100.00
D18	FB	−0.4	61.2	0.791	15.40	7.49	0.09	2.78	1.55	3.19	4.39	3.00	99.88
D18m			61.7	0.6	15.0	6.2	0.1	2.8	2.6	3.2	4.2	3.7	99.9
D18sd			0.6	0.2	0.6	1.8	0.0	0.0	1.5	0.0	0.3	0.9	0.1

B1 and D18 had duplicate analyses and mean (m) and standard deviation (sd) are reported.

see Section 3.2). The fault and wall rocks have a range in the power-law exponent, D, from 2.43−3.31: hanging-wall samples from $D = 2.45$−2.52, footwall samples from $D = 2.43$−2.63, damage-zone and foliated-breccia samples from $D = 2.77$−2.79, and gouge samples have a broad range from $D = 2.86$−3.31 (see also Morgan et al., 1996). Power-law PSDs are generally calculated across a grain size range of ~1−100 μm. Yet, it is important to emphasize that the higher power-law exponents (i.e. $D > 3$) reflect a deficiency of particles >63 μm, and an abundance of particles <2 μm. For example, clay gouges can have as much as 62 wt.% <2 μm, although 15−20 wt.% is more representative. The PSD data from the Black Mountain fault rocks are consistent with PSD data from other natural and experimental fault zones (Mair et al., 2002; Hadizadeh and Johnson, 2003; Storti et al., 2003) in that a range of D-values exists in cataclasites and gouges. Power-law PSDs provide insight into the mechanical history of fault rocks (Sammis et al., 1987; Wilson et al., 2005; Chester et al., 2005), as discussed in a following section.

6. Mineralogy

The mineralogy of the fault rocks can be separated into that of the clasts and the matrix. Previous work has shown that the clasts are >60% to as much as 90% quartz and feldspar (Mormon Point and Badwater samples), or have the more heterogeneous mineralogy of mica-rich schists and carbonates (Copper Canyon and Badwater samples) (Hayman et al.,

Table 4
Stable isotope data for three grain-size separates: <2 μm (C), <0.2 μm (M), 0.02 μm (F) Calculated initial water compositions assuming fractionation factors of Savin and Lee (1988)

Sample	Position	Rock-type	Size	δ180	Δ water-smectite, 50 °C	Δ water-smectite, 100 °C
A-24	0	CG	C	10.1	−10.41	−4.28
A-24			M	10.4	−10.12	−3.98
A-24			F	12.7	−7.87	−1.72
A-25	−0.4	G	C	6.4	−14.03	−7.92
A-25			M	6.5	−13.98	−7.87
A-25			F	8.1	−12.36	−6.24
A-27	−0.1	FB	C	10.5	−10.02	−3.89
A-27			M	11.5	−9.04	−2.90
A-27			F	13.0	−7.57	−1.42
A-49	−0.4	G	C	9.5	−11.00	−4.87
A-49			M	10.7	−9.82	−3.69
A-49			F	12.7	−7.87	−1.72
A-55	−0.4	FW	C	10.1	−10.42	−4.29
A-55			M	10.9	−9.60	−3.46
A-55			F	11.1	−9.39	−3.26
B-1a	−0.2	CG	C	11.7	−8.85	−2.70
B-1a			M	11.5	−9.04	−2.90
B-1a			F	11.6	−8.94	−2.80
B-1b	−0.2	CG	C	11.4	−9.14	−3.00
B-1b			M	10.7	−9.82	−3.69
B-1b			F	11.4	−9.14	−3.00
D-2	−0.1	G	C	12.1	−8.45	−2.31
D-2			M	11.7	−8.85	−2.70
D-2			F	13.9	−6.65	−0.50
D-18	−0.4	FB	C	8.7	−11.78	−5.66
D-18			M	9.0	−11.50	−5.37
D-18			F	12.1	−8.47	−2.33

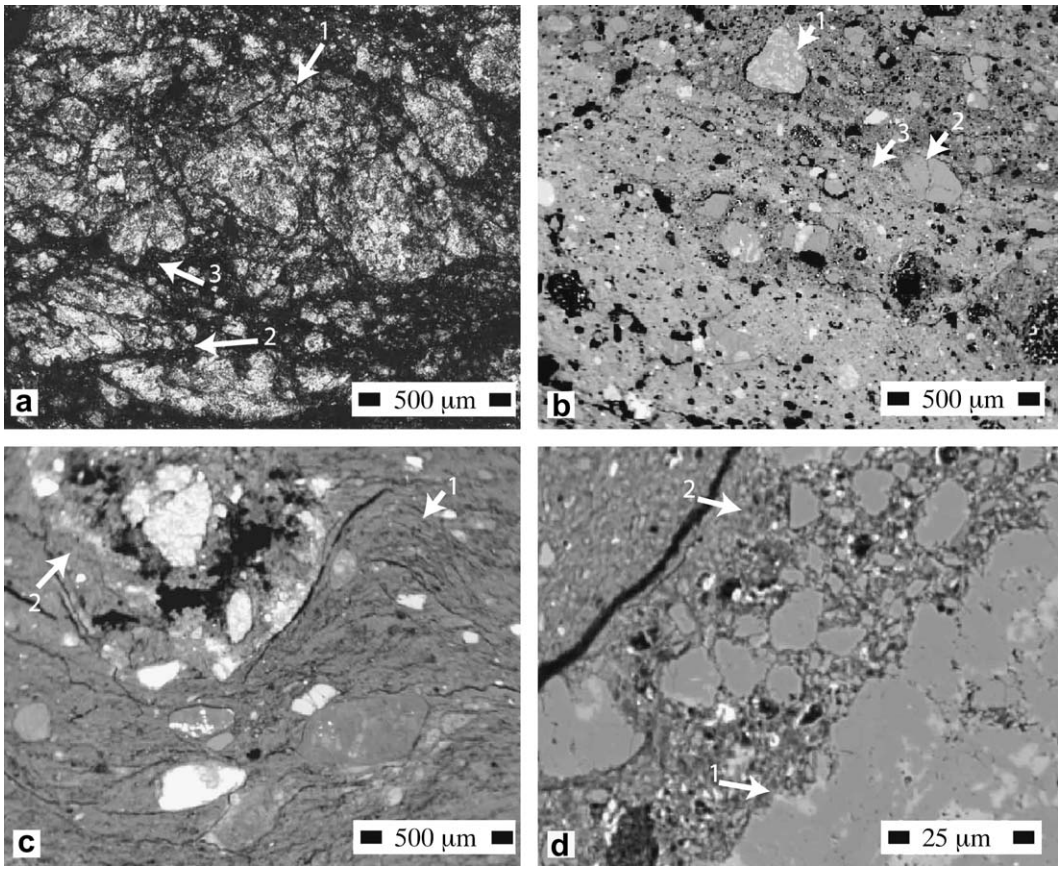

Fig. 4. Microstructure of fault rocks: (a) Photomicrograph in plane-polarized light of a foliated breccia. (1) The central area of the photomicrograph is a large clast of altered diorite riddled by transgranular fracture. (2) A transgranular fracture cuts across a clast. (3) Abraded grain boundaries and granular domain between larger clasts. (b) SEM (in BSE mode) image of a gouge. (1) Smooth grain boundary of a survivor grain. (2) Transgranular fracture does not trace into surrounding matrix (i.e. predates gouge deformation). (3) Compositional microbanding indicated by grayscale (atomic weight is proportional to the grayscale). (c) SEM (in BSE mode) image of scaly clay gouge. (1) Anastamosing scaly foliation. (2) Large clast in the center of the image is likely a reworked clast of fault rock. (d) SEM (in BSE mode) image of a gouge. (1) Abraded grain boundary. (2) Disseminated clasts form a ~25 μm domain surrounding the grain boundary.

2004). The dominant constituents of the matrix are phyllosilicates, namely illite, chlorite, illite-smectite, and chlorite-saponite (Table 2). None of the interstratified phases are ordered (the Reichweite ordering is 0), although the proportion of swelling clays (smectite and saponite) varies between samples.

Non-phyllosilicate mineral constituents of the matrix have been identified by XRD including variable amounts of albite, orthoclase, calcite, dolomite, quartz, and hematite. Previous work showed that some illite grains contain nanometer scale inclusions of magnetite and carbonate (Hayman et al., 2004)

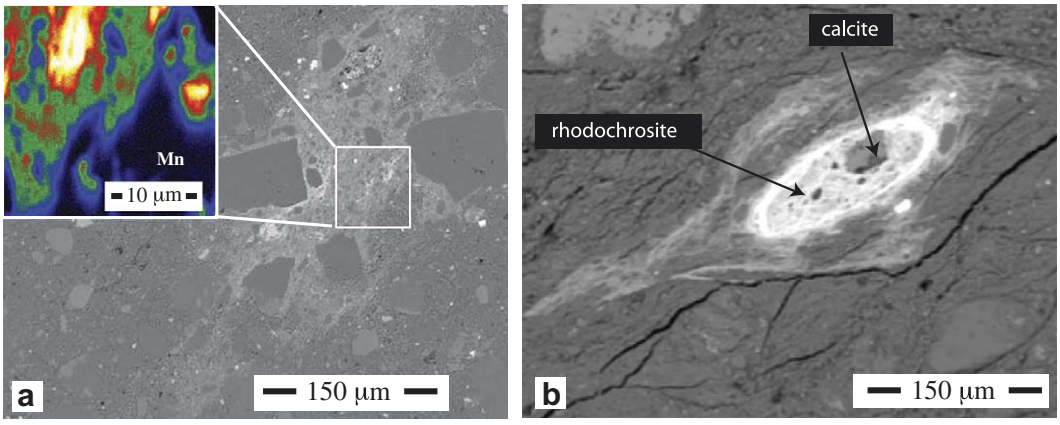

Fig. 5. Manganese halos: (a) Unstrained halo of manganese oxide. The inset is an X-ray map of manganese distribution for the upper right area of the boxed region. (b) Strained manganese-carbonate-halo.

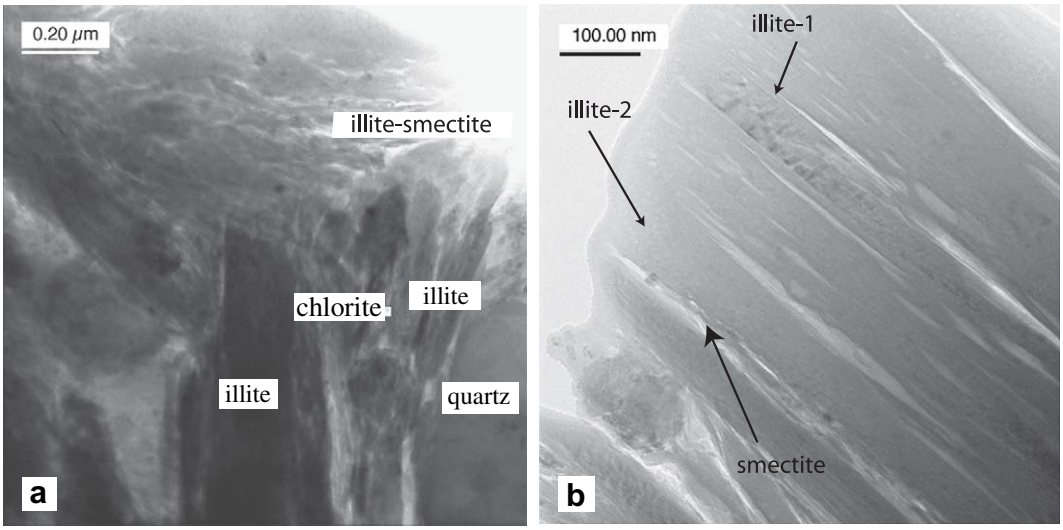

Fig. 6. TEM of gouge matrix: (a) illite, chlorite, and illite-smectite (note irregular, light patches in otherwise gray areas of the image) ''wrap'' around a quartz grain (lower-right corner). (b) A single grain exhibits a central, slightly strained illite (illite-1), surrounded by unstrained illite with less well-defined lattice fringes (illite-2), and lenticular lattice fringes, smectite.

and reconnaissance TEM identified grains of blocky orthoclase and other silicate and non-silicate minerals mixed with Cu- and S-bearing gels (cloudy electron diffraction patterns were observed) (Hayman, 2003). At the meso- and microscales iron and manganese oxides and carbonates have been visually identified, including magnetite, siderite, and rhodochrosite (see Section 2.3). The iron and manganese oxides form halos (see Section 4) and also fill fractures and coat grain boundaries.

There are some systematic variations in the mineralogy of the clay-sized component between localities and rock types. The hanging walls are deficient in many of the phases that enrich the fault and footwall rocks. The shear bands, and the Badwater detachment's principal slip plane in particular, have a distinctive mineralogy dominated by calcite; oxides and silicates have been observed in other shear bands. However, the mineralogy does not vary greatly between the footwall, breccia, and gouge, except insofar as there are proportionally more matrix minerals in gouge. As a rule, the matrix mineralogy of Badwater and Mormon Point detachments contains illite, illite-smectite, and chlorite. Copper Canyon is unique in that illite and smectite are absent overall, and a crystallographically distinctive (''turbo-stratified'') chlorite-saponite enriches the gouge, possibly imparting the scaly fabric.

The fault rocks therefore have an abundance of alteration minerals, largely phyllosilicates in the <2 μm fraction. As noted in a previous paragraph, the detachment footwalls have a similar mineralogy as much of the fault zone. A notable exception is within damage zones in the footwall where ''bleached'' areas are relatively poor in mafic minerals (Fig. 2a). Also found in damage zones are veins of siderite (Fig. 2b), hematite, or tourmaline, and areas rich in chlorite and epidote (Byrnes, 1989; Cowan et al., 2003). Gouge units cut all of the veins and mineralized domains in the footwall (Fig. 2b). These characteristics show that fluid-rock reactions in the footwall of the detachments were an important component of the early history of the shear zones.

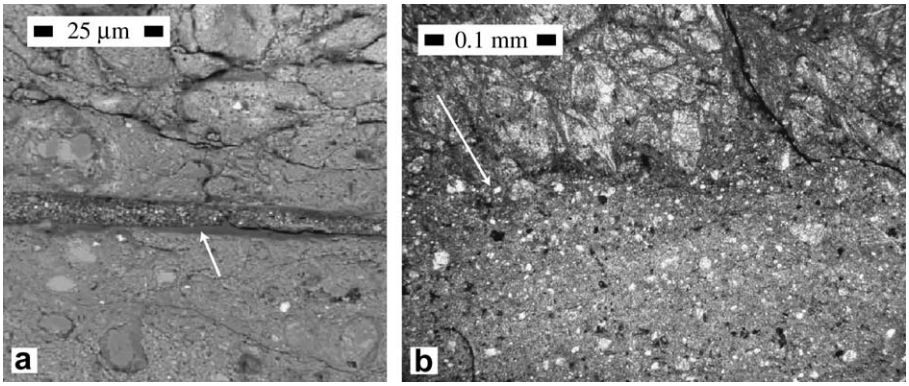

Fig. 7. Shear bands (indicated by arrows): (a) SEM (BSE-mode) image of a Y-oriented shear band within Copper Canyon gouge. Reconnaissance EDS of the ~10 μm wide band produced only potassium and aluminum k-α peaks. (b) Photomicrograph in plane polarized light of a principal slip plane from the Badwater detachment. The PSP is compositionally and mineralogically distinctive and dominated by calcite. Other shear bands, and riedel shears in particular, are enriched in opaque minerals such as manganese and iron oxides.

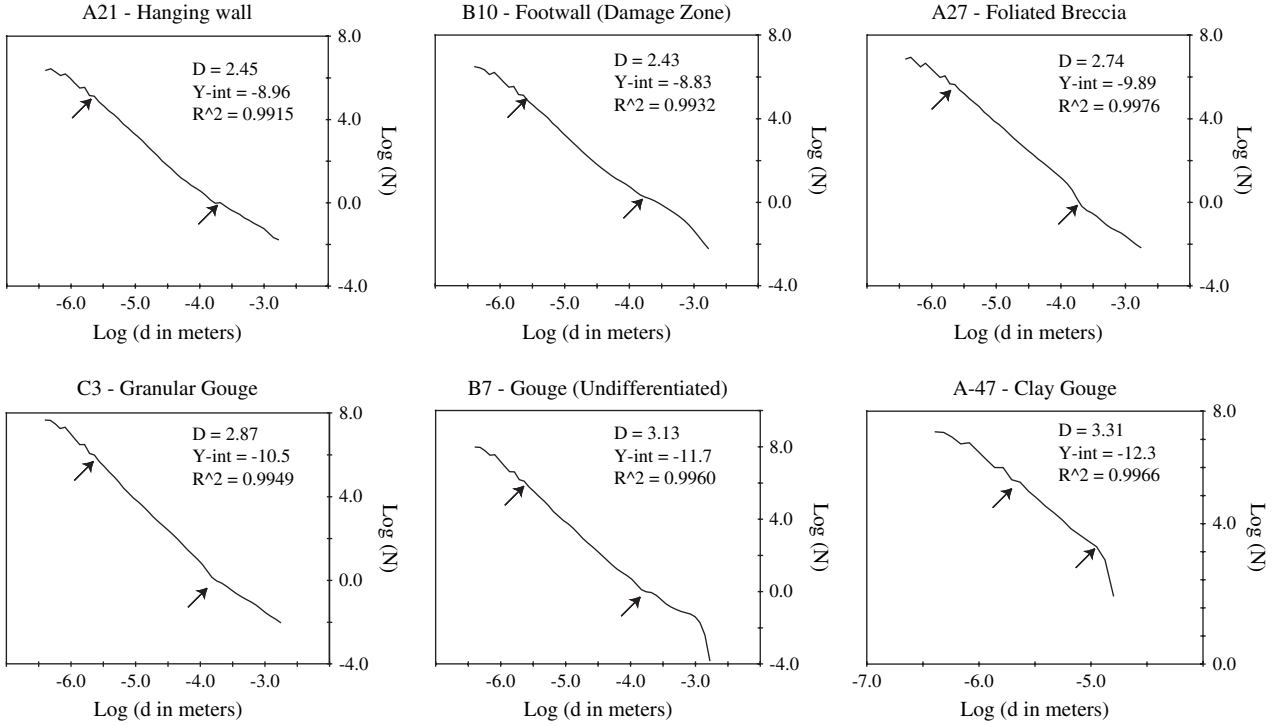

Fig. 8. Power-law PSD spectra for 6 representative samples; all PSD data are tabulated in Table 1 along with weight percent of specific size fractions. The horizontal axis is the logarithm (base 10) of the clast diameter (d) in meters. The vertical axis is Log (cumulative number). Arrows denote approximate limits of LPSA resolution. Near the lower limit, ~2 μm (just above "−6"), the LPSA data have a staircase pattern due to some combination of instrument behavior and sample preparation such as flocculation. At ~100 μm the LPSA approaches its limit of resolution, primarily because the cumulative number of particles >100 μm ("−4") is increasingly small. For example, sample A47 has very few grains larger than 10 μm, and the break in power-law slope reflects that.

7. Fault-rock compositions

As indicated by their mineralogy, the Black Mountain fault rocks have a range of compositions that prevents straightforward correlations between fault and wall rock units and assessment of statistical variance in the compositions. The only method available is to study the composition of representative samples relative to one another, providing a general view of compositional variation across the detachment shear zones (e.g. Cowan et al., 2003).

Elemental compositions have a wide range of values at individual localities, and vary between localities (Table 3). For example, Copper Canyon samples have major element compositions that vary by as much as 26.2 wt.% for SiO_2, with compositional variability of <1 wt.% for only TiO_2 and MnO. The loss-on-ignition (LOI) and MgO are also variable between fault rocks, with the most pronounced enrichment in the chlorite-saponite bearing scaly gouges. In comparison with the Copper Canyon samples, the Mormon Point samples are relatively uniform with compositional variations between samples of <10 wt.% for most elements. Given the matrix mineralogy dominated by illite and illite-smectite, it is noteworthy that the Mormon Point gouges are enriched in LOI, and have comparable concentrations of K_2O, Na_2O, Fe_2O_3, and rather uniform MgO concentration between samples. Samples from Badwater have some of the same properties as Mormon Point. However, the principal slip plane, sample D14, is compositionally unique, with depletion in SiO_2 and enrichment in CaO and LOI of $\gg$10 wt.%.

The raw element weight percents only crudely allow comparison of fault and wall rock compositions. A better way to compare rock compositions is with concentration ratio diagrams (Fig. 9). The diagrams display the ratio of the concentration of a given element in one rock to another:

$$R_{\text{element}} = \frac{C^{\text{fault-track}}_{\text{element}}}{C^{\text{wall-rock}}_{\text{element}}} \quad (\text{e.}g.,\ \text{Ague},\ 2003)$$

If $R = 1$ *and* there were no mass or volume changes associated with chemical reactions, than the element was invariant to any changes associated with fault-rock development. Thus, the concentration ratio diagram is roughly equivalent to an isocon diagram (Grant, 1986) but without the inherent problems that arise with scaling factors and linear regressions across a range of values (Ague and Van Haren, 1996).

The samples from Mormon Point have the simplest concentration ratio diagram. All of the elements with the exception of MnO and CaO have ratios that scatter around unity, with some of the Mormon Point fault-rock samples having a high R_{MnO} and R_{CaO} relative to footwall samples. Samples from Badwater also have concentration ratios that scatter around unity. Exceptions to this are ratios between fault rocks and hanging-wall sample D22 (R_{MnO}, R_{MgO}, and R_{LOI} are all >10) and ratios between the principal slip plane and footwall samples ($R_{\text{CaO}} = 13.22$ and $R_{\text{LOI}} = 8.25$).

In contrast with Badwater and Mormon Point, samples from Copper Canyon have a range of concentration ratios

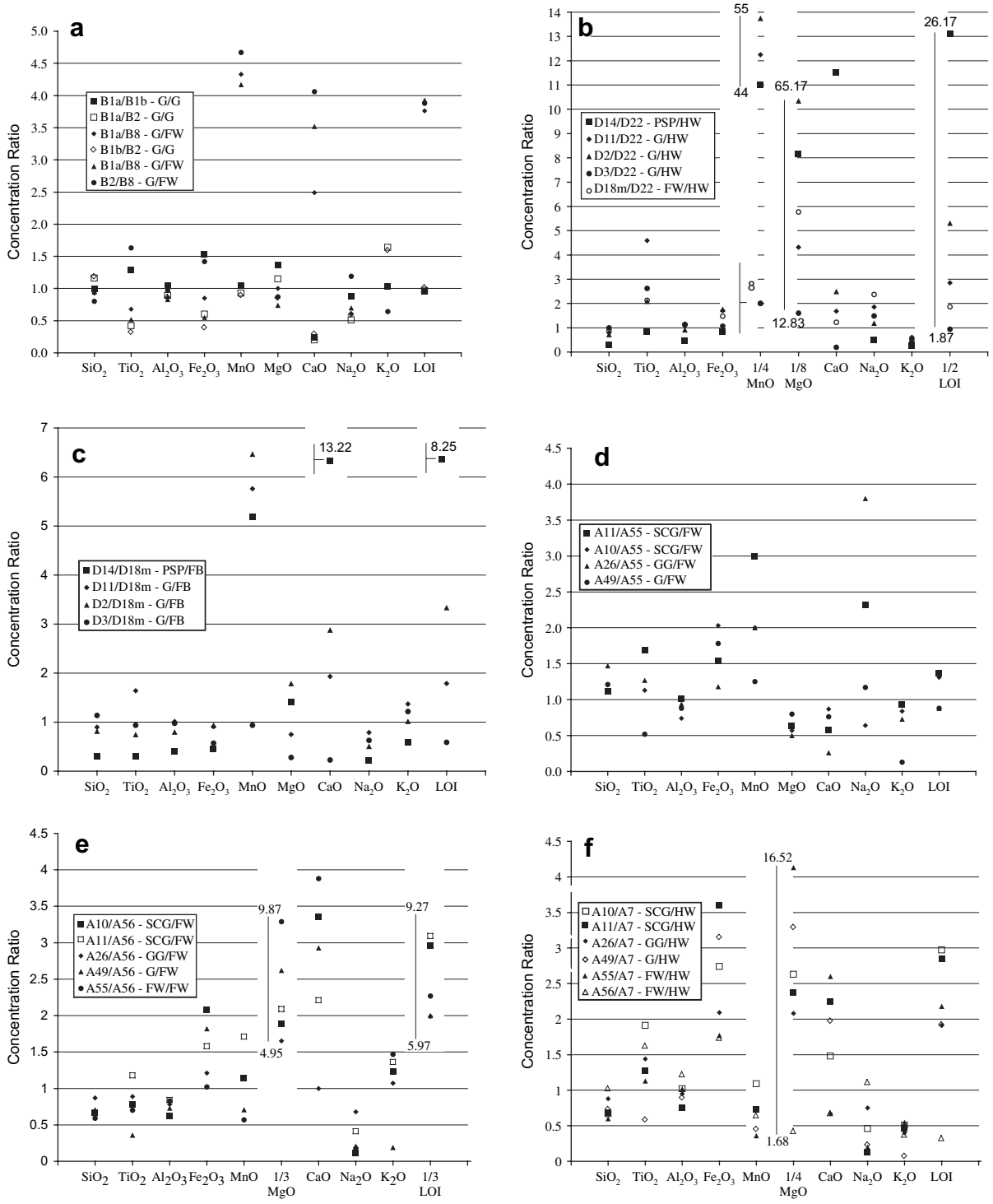

Fig. 9. Concentration ratio diagrams wherein the ratio of the concentration of a particular rock against another is plotted for the suite of major elements. Scaling factors are used for specific elements only for graphical clarity. (a) Mormon Point ratios include ratios of fault-rocks compositions to one another. (b) Badwater ratios between fault rocks and the hanging wall. (c) Badwater ratios between fault and footwall rocks. (d) Copper Canyon ratios between fault and mafic footwall rocks. (e) Copper Canyon ratios between fault and felsic footwall rocks. (f) Copper canyon ratios between fault and footwall rocks and the hanging wall.

that largely indicate a heterogeneous footwall. For example, when compared with mafic footwall sample A55, the fault-rock concentration ratios are between 0 and 2, except for R_{MnO} and R_{Na2O} with values up to 3 and 4, respectively. However, when compared with felsic footwall sample A56, the fault-rock concentration ratios are much more variable with R_{MgO} and R_{LOI} up to 9.87 and 9.82, respectively. The latter range of concentration ratios is consistent with the abundance of the chlorite-saponite in the Copper Canyon clay gouge. Lastly, comparing the Copper Canyon fault rocks with the

hanging wall shows that there is little correlation between the two.

One might argue that a robust correlation between samples must be made before concentration ratio diagrams can be properly interpreted (Ague and Van Haren, 1996), and indeed certain reference samples, particularly from the hanging wall, are not well correlated with fault-rock samples. Yet, the comparison of fault- and wall-rock compositions indicates that several elements (MnO, MgO, CaO, LOI) have systematic concentration ratios in the fault rock relative to the footwall. The concentration ratios are thus consistent with petrography, mineralogy, and field data that find that minerals rich in these elements have spatially heterogeneous, but somewhat systematic, distributions. This is explored further, following a presentation of data that bear on the source of reactive fluids within the detachments.

8. Oxygen isotope composition

The stable oxygen isotope data from <2 μm, <0.2 μm, and <0.02 μm separates show a range of $\delta^{18}O$ values from 8.7‰ to 13.9‰ (Table 4). There is no systematic enrichment or depletion in $\delta^{18}O$ between fault-rock samples or between fault and wall rock; no hanging-wall samples were analyzed. With the exception of Mormon Point sample B1, finer grain sizes produce higher $\delta^{18}O$ values with systematic differences between the size fractions of up to several per mil.

The stable oxygen isotope composition has no systematic variation across the fault zones and between localities, indicating that the nature of the reacting fluids did not change systematically over space. Assuming that all of the matrix minerals did not grow instantaneously, then the fluids did not change greatly over time. The compositions therefore give us additional information about the composition of the fluids that passed through the shear zones, but do not indicate the more complicated history of changing source waters or temperature during alteration reported for other detachments (Losh, 1997; Morrison and Anderson, 1998).

9. Discussion

The investigation of the Black Mountain detachments was largely motivated by a desire to understand their mechanical history. For example: did elevated fluid pressure, low-friction minerals, or some other mechanism, weaken the detachments? Another motivation was to see if it was possible to determine if particular fault-rock structures resulted from aseismic, stable creep (Cowan, 1999). Although these lofty goals were not truly met, the acquired data provide a great deal of insight into the history of the fault rocks. In order to properly integrate the data sets, a thorough geochemical, mineralogical, and structural treatment is presented in the following sections, including a synthesis into a conceptual model and brief discussion of the mechanical implications.

9.1. Water-rock history

Some fault zones worldwide have fault-rock units that contrast enough in composition to allow quantitative modeling of reaction progress and changes in mass (Manatschal et al., 2000; Yonkee et al., 2003). The fault rocks in the Black Mountain detachments do not have such definitive compositions and because of the micron-scale grain sizes of many of the authigenic minerals, abundant quantitative mineral chemistry is not readily attainable. Despite the lack of diagnostic fault-rock compositions or near-equilibrium mineral assemblages, the reaction history within the detachments can be crudely estimated with a useful activity diagram constructed by Helgeson et al. (1979) (Fig. 10a) (after Vrolijk et al., 1997).

The activity diagram shows two aspects of the fault-rock history with respect to water. Firstly, the absence of kaolinite shows that fluid compositions were restricted in the variation of aK^+. In other words, hypothetical reactions involving kaolinite and chlorite or muscovite were not equilibrium reactions and went to completion. A consequence was that the altering fluids caused the growth of illitic minerals without increasing the concentration of potassium in the rock. Secondly, the system, while closed to large changes in aK^+ and aH^+, was open with respect to changing aMg^{++}, consistent with the observed enrichments in fault-rock MgO and LOI that are controlled by chlorite and the smectite/saponite minerals. The Mg^{++}_{aq} for the reactions might have been liberated from dolomite (Yonkee et al., 2003), or from the damage zones that show depletion in mafic minerals (see Section 6). Alternatively, enrichment in the Mg^{++}_{aq} was from surficial waters.

This concept of "enrichment" versus "depletion" of elements assumes that any change in mass of the bulk rock was negligible. One index of mass change is the concentration ratio of immobile elements (Ague, 2003). Al_2O_3 is present in a variety of phases, and is a balancing component of phyllosilicate-involved reactions leading to its consideration as an immobile element and a good indicator for geochemical variability and mass-changes (Gresens, 1967). Al_2O_3 has a very restricted range of concentration ratios with: 0.8–1 (Mormon Point), 0.8–1 (Badwater, not including the principal slip plane), and 0.7–1 (Copper Canyon). According to this interpretation, the net loss of mass was as much as 30%, but more typically <10%, and the net gain was negligible.

9.2. Nature of fluids

The available stable isotope data provide further information about the nature of the fluids. The fault rocks exhibit a systematic shift in $\delta^{18}O$ with grain size, best explained by the fractionation of ^{18}O relative to ^{16}O by matrix minerals. An estimation of the original water composition is thus available, assuming that illite, chlorite, and smectite are responsible for this fractionation. The fractionation factors (α) for smectite and chlorite (illite would fall between the two) are (Savin and Lee, 1988):

$$\alpha_{\text{smectite-water}} = 2.58 \times 10^6 T^{-2} - 4.19$$

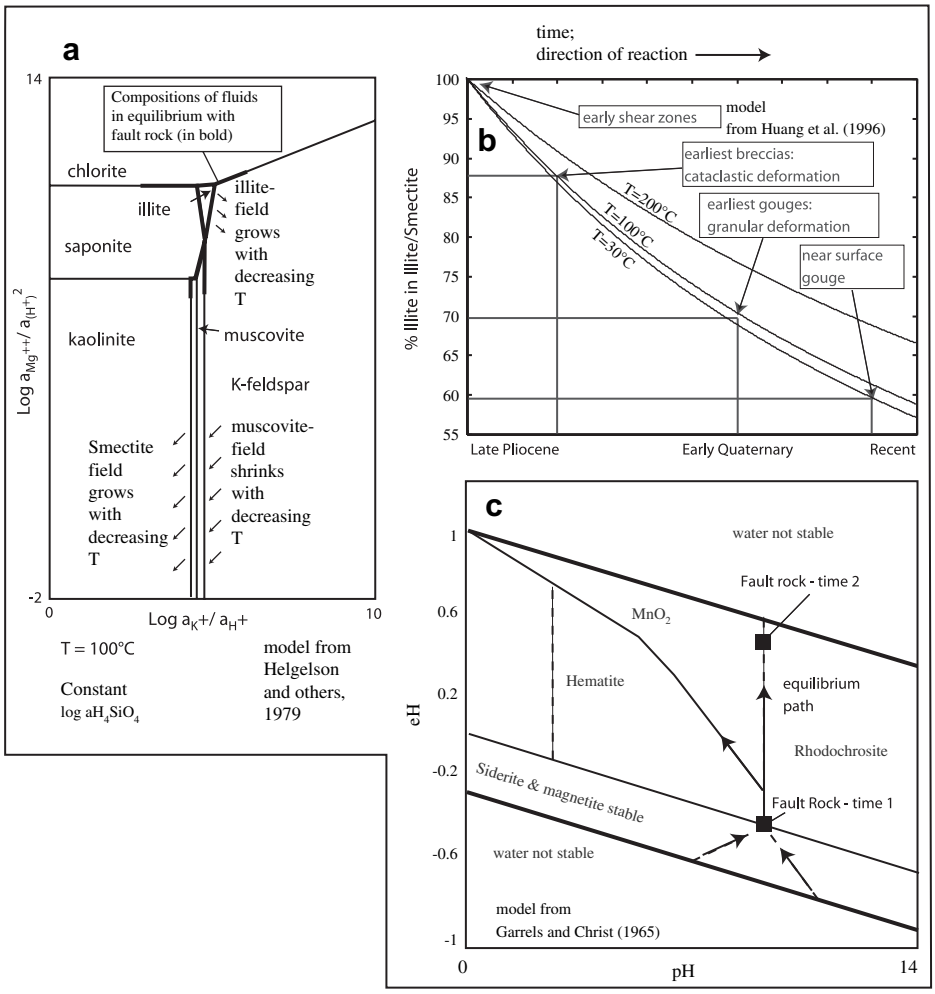

Fig. 10. Three geochemical approaches to interpreting the fault-rock history: (a) Activity diagram from Helgeson et al. (1979). The major equilibrium lines of the diagram are defined by reactions between kaolinite, muscovite, chlorite, and feldspar, the relevant aqueous cations (K^+, Mg^{++}), pH control (H^+), silica in its stable aqueous form (H_4SiO_4), and water. (b) Numerical solutions for the experimentally derived illite-smectite rate law of Huang et al. (1993). Time is non-dimensional: in the experiments the transition occurred over the order of days, whereas in the detachments it is proposed to take place over the late Pliocene and Pleistocene. (c) After Chan et al. (2000) and Garrels and Christ (1965), the oxidation potential (eH) versus pH with stability fields for siderite, magnetite, hematite, rhodochrosite, and MnO_2. The arrow shows the relative timing of the different oxides and carbonates indicated by crosscutting and other structural relationships.

$$\alpha_{\text{chlorite-water}} = 2.56\times10^{3}T^{-1} + 3.39\times10^{6}T^{-2} - 0.623 \times 10^{9}T^{-3} + 0.056\times10^{12}T^{-4} - 11.86$$

Assuming a temperature of 50–100 °C (see Section 9.3), the equivalent ranges for the composition of the water are from −0.5‰ to −7.52‰ (smectite fractionation) and −3.85‰ to +3.61‰ (chlorite fractionation). The calculated values are heavier than the 13.5 to −9.5‰ post-Sierra Nevada basin-and-range water (Feng et al., 1999). Possibilities for the increase in $\delta^{18}O$ relative to basin-and-range water are that meteoric water has changed throughout the Plio-Pleistocene or that the altering fluids had a long residence time in the detachment basins. The explanation favored here is that the $\delta^{18}O$ reflects mixing of low-temperature silicates with silicates inherited from earlier, higher temperature alteration.

The roughly meteoric $\delta^{18}O$ shows that the fluids did not equilibrate with the silicate and carbonate wall rocks and survivor grains, yet the geochemistry shows that the reactions between the water and rocks was somewhat restricted. It is thus inferred that the volume of fluid entering into the fault zone was large, but was accessed from low-temperature near-surface waters.

9.3. Mineralogical indications for temperature and fluid evolution

The inferred temperature of isotope fractionation partly comes from the ~3 km thickness of the detachment sedimentary basins in the modern environment (Blakely and Ponce, 2001) and a modern geothermal gradient of <30 °C/km (Sass et al., 1994). There is however, an independent estimate of the thermal history of the fault rocks in the form of an experimentally derived rate law for clay mineral transitions (Huang et al., 1993):

$$-\frac{\mathrm{d}Sm}{\mathrm{d}t} = Ae^{(-Ea/RT)}[K^+]Sm^2$$

where Sm is the % smectite in illite-smectite, $[K^+]$ is the concentration of potassium in solution, Ea is the activation energy, R is the gas constant, and T is temperature (Fig. 10b). There is no readily applicable rate law for the chlorite-saponite transition. Only very large changes in $[K^+]$ affect the illite-smectite transition and concentration ratios between fault and wall rock are low for potassium. Thus temperature is more important than fluid composition in driving the transition.

An important microstructural observation in this context is the presence of illite-smectite matrix grains that have highly ordered, well-defined lattice fringes surrounded by less well-defined lattice fringes that are free of internal strain and contain the smectitic layers (see Section 4). An interpretation of these grains is that the slightly strained lattice fringes belong to an earlier, higher temperature muscovitic illite that began to grow at temperatures ~100 °C. With decreasing temperature the interstratified illite-smectite lattice fringes developed and were never subjected to minor intercrystalline strain (Fig. 10b).

Crosscutting relationships in the field also provide information on the changing conditions of mineralization. Siderite veins predate much of the fault rock, and predate all of the gouge development (see Section 2.3). The fault rocks contain magnetite grains that grew within illite-smectite grains (Hayman et al., 2004). Lastly, texturally young iron and manganese oxides form alteration halos (Section 4). Manganese oxides of the type described here are stable in the presence of oxidizing water, whereas siderite and magnetite require relatively reducing conditions (Fig. 10c) (Garrels and Christ, 1965; Chan et al., 2000). Thus, the change from texturally early oxides and carbonates to texturally late oxides requires an increase in oxidizing potential (eH) of the altering solution to near-surface values (Fig. 10c). Such a change is consistent with the down-temperature history predicted by the clay mineral assemblage.

9.4. Microstructure

In most places along the Black Mountain detachments, granular textures, more prominent in the gouge, crosscut or overprint cataclastic textures, more prominent in the breccia. An interpretation of the relationship is that granular flow (via interparticle slip) dominated over cataclasis (via transgranular fracture) as the shear zone evolved. In contrast, several workers have proposed that fracture at the sub-micron scale is the dominant mechanism throughout gouge development (Wilson et al., 2005; Chester et al., 2005). The TEM and SEM images do not provide any direct evidence for fracture within the micron-scale matrix — unless one considers frictional slip a fracture phenomena (e.g., Beeler, 2004) — but do display granular textures such as strained halos, shape-preferred orientations (Cladouhos, 1999a,b; Hayman et al., 2004), and compositional microbanding (see Section 4). Furthermore, many of the grain sizes approach an experimental grind limit at which silicates are less efficiently comminuted (An and Sammis, 1994; Cho et al., 1996; Hadizadeh and Johnson, 2003). Yet, the gouges have a range of PSDs, and abraded grain boundaries are a prevalent microstructural feature. In other words, comminution of gouge continued even after granular flow became the dominant deformation mechanism.

Several proposed models help explain the observed power-law PSDs and relevant microstructures. *Constrained comminution* occurs by incremental transgranular fracture, producing $D \approx 2.6$ at some critical shear strain (Sammis et al., 1987). A recent modification of the constrained comminution model holds that at some critically low normal stress, grain-boundary abrasion yields higher D-values (Storti et al., 2003; Rawling and Goodwin, 2003). The microstructures of the fault rocks are consistent with each of these models. The cataclastic breccias, with $D = 2.77–2.79$, contain evidence for constrained comminution, whereas the granular textured gouges, with $D = 2.86–3.31$, contain evidence for grain-boundary abrasion. In some experiments changes in PSD occur as a function of normal stress (σ_n), from $\sigma_n = 50$ MPa to $\sigma_n = 5$ MPa with a concomitant increase in the roundness of grains, and decrease in the coefficient of friction (Mair et al., 2002). The equivalent change in normal stress in the Black Mountain detachments would have been due to exhumation from roughly 2 km depth. In turn, the D-values increase toward the PSP, consistent with the hypothesis that D-values reflect increasing finite shear strain (Hadizadeh and Johnson, 2003) (Fig. 11).

The PSD and microstructural variation in the Black Mountain fault rocks therefore indicate that deformation proceeded with decreasing confining pressure and increasing finite shear strain, and gouge development dominated above ~2 km depth. The PSP is also compositionally distinct, indicating that chemical processes within the fault zone were sensitive to this strain localization. Strain localization of the kind described here likely reflects a strain softening history for the shear zones (Means, 1995), and provides an important linkage between the structure, composition, and mechanical history of the shear zones.

9.5. Conceptual model and implications

A conceptual model is proposed here that envisions fault-rock development throughout the denudation history of the Black Mountains (Fig. 12). By 3.1 Ma the detachments were at <3 km depth (see also Section 2.1 and 2.2) in the presence of fairly reducing meteoric fluids. The foliated breccia began to develop via constrained comminution. Between 3.1 Ma and early Quaternary time, illite-smectite and chlorite-saponite grew with decreasing temperature. During this interval the gouge developed and granular flow, including interparticle slip and grain-boundary abrasion, dominated over cataclastic flow and constrained communition. Continued denudation of the turtlebacks brought the detachments to uppermost crustal levels where Mn-oxides and other near-surface minerals were stable. Strain localization throughout the shear zones' history culminated with development of the PSP and other texturally and compositionally distinctive shear bands. However, distributed, granular flow continued after localization as shown by the strained oxide aggregates and lenses of Pleistocene hanging-wall sediment within the shear zones (Cowan et al., 2003).

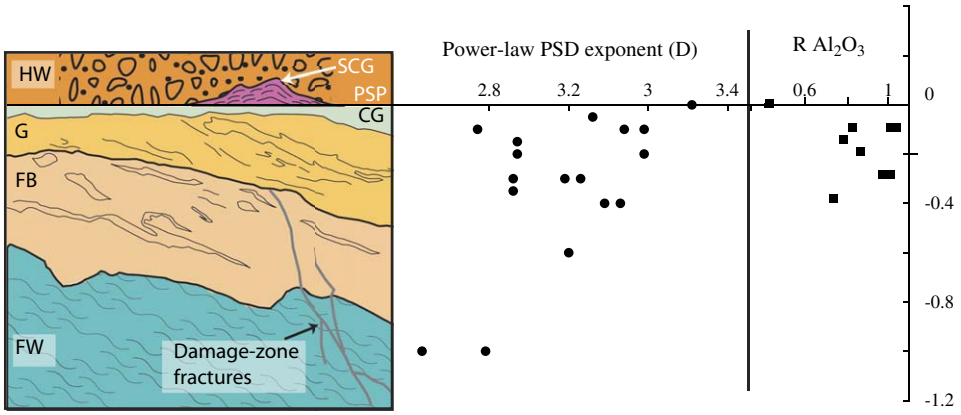

Fig. 11. Schematic of a Black Mountain detachment. Power-law exponents (D) increase from $D < 3$ to $D = 3.31$ upward toward the PSP, although D has a considerable range at all positions. RAl_2O_3 has a range between 0.8 and 1 at all positions in the shear zone, but exhibits a weak qualitative trend downward toward the PSP, which has an anomalously low RAl_2O_3. RAl_2O_3 provides a rough estimate of mass change and the overall geochemical variability.

If, as proposed, the detachment shear zones evolved over geologic time and across basin depths, then fault rocks were developing across time intervals when the detachments were frictionally weak ($\mu < 0.4$) and intervals when they were strong ($\mu > 0.4$) (Section 2.2). Worldwide, syntectonic veins, large compositional variations and isotopic anomalies across shear zones are cited geological evidence for fault-weakening through elevated fluid pressure (Chester et al., 1993; Yonkee et al., 2003). Indeed, slip on two active low-angle normal faults is explained through the interaction of elevated fluid pressure and hanging-wall faults (Kopf, 2001; Collettini and Barchi, 2002). An alternative mechanism for weakening is the growth of low-friction minerals. For example, a recent experimental study of fault gouge from detachments in Panamint Valley, CA, found that samples with >50% total clay content were weak ($\mu < 0.4$) (Numelin et al., 2004).

Evidence for elevated fluid pressure in the Black Mountain fault rocks is scant; they are devoid of syntectonic veins (Cowan et al., 2003), and there is not a well-defined compositional anomaly across the detachment shear zones. There are a variety of arguments that faults that fail via elevated fluid pressure should cause migration of fluids up-dip from deeper crustal levels (e.g., Faulkner and Rutter, 2001). Despite the evidence for fluids having been abundant within the detachments, no isotopic fingerprint for deeper crustal waters has been identified. Admittedly, it is possible that fluid pressures were elevated from hydrostatic at the grain scale without leaving a geologic record. But without more evidence, it is reasonable to explore some other fault-weakening mechanisms. More certain, for example, is the enrichment in clays and clay minerals within the fault rocks, including smectitic/saponitic clays long shown to have low friction (Byerlee, 1978). Yet, the fault-rock mineralogy is heterogeneous, and only Copper Canyon gouge has clay content of several tens of percent. Given that friction increases in proportion to the amount of non-clay content (Saffer and Marone, 2003), it seems overly simplistic to claim that clay minerals were the primary control on the Black Mountain detachments' strength, although they were no doubt important.

In summary, there is a general, albeit uncertain sense that the grain-scale friction and fluid pressure within the fault rocks were important influences on detachment strength but neither appears to be an entirely satisfactory explanation for fault weakening. A possible route to a more satisfactory understanding of detachment mechanics is an exploration of dynamic weakening. Numerical and rock mechanics experiments have shown that textural properties such as the roundness of grains and PSD exert a strong influence on dynamic strength by facilitating particle rotation and strain localization (Morgan and Boettcher, 1999; Morgan, 1999; Mair et al., 2002). These controls on friction presumably contribute to seismic slip and can feedback to influence the static friction (Anthony and Marone, 2005). The Black Mountain detachments contain abundant evidence for particle rotation, evolving PSDs, and strain localization over geologic time. Thus, the data presented here inspire the hypothesis that detachment strength was modified by granular flow of the fault rocks. The granular-mechanics hypothesis, though broad, has implications for understanding the distribution of seismicity and changes in fault rheology with depth.

10. Conclusions

Integration of field, microstructural, mineralogical, and geochemical data elucidates the time-depth history, deformation mechanisms, and the water-rock interaction within the Black Mountain detachment shear zones. The shear zones evolved with denudation of >3 km of sedimentary basin cover from the Black Mountains, from late Pliocene to Recent time. Granular-textured gouges postdate cataclastic breccias, and the gouges have higher power-law PSD exponents. The textural differences coincide with a finite strain gradient that increases toward shear bands. Authigenic minerals required water-rock reactions, but net compositional variation is small relative to other fault zones described in the literature. Stable isotope compositions reflect clay mineral fractionation of meteoric water. Water was therefore abundant, but significant deeper crustal fluid did not enter into the shear zones. Field

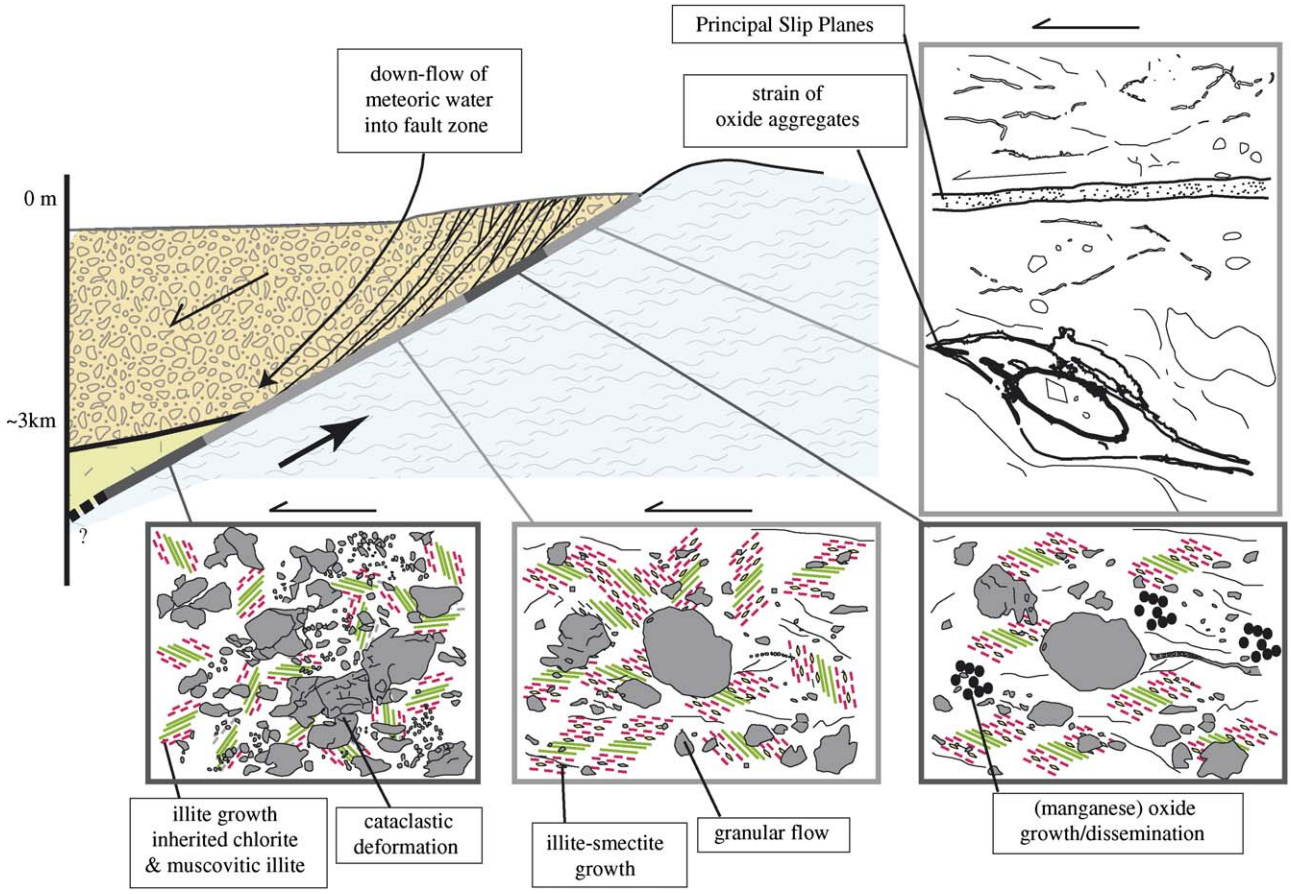

Fig. 12. A geologic model for the evolution of the Black Mountain fault rocks. By late Pliocene time the fault rock was exhumed to ~3 km depth and accommodated strain by cataclastic flow, producing foliated breccias. Illite grew stably, and muscovitic illite and chlorite were mechanically inherited from earlier alteration. Between the late Pliocene and Recent time the detachments reached uppermost crustal depths, denuding the Black Mountains and extending the hanging walls. Gouges were present and accommodated strain via granular flow. Illite-smectite (and chlorite-saponite) grew, fractionating meteoric water that flowed down detachment and hanging-wall fault planes. In Recent time and near the surface, oxides were disseminated in alteration halos, and subsequently strained. The (most recent) shear bands developed, including the principal slip plane.

constraints show that the protracted history of the fault rocks includes intervals during which detachment strength was weak and slip was possibly seismogenic. The different frictional deformation mechanisms, water-rock reactions, and mineral transitions obscure identification of specific weakening-mechanisms. Via analogy with theory and experiment, the Black Mountain detachments were likely dynamically weakened by granular flow.

Acknowledgements

Darrel Cowan, Julia Morgan, Trenton Cladouhos, and Peter Vrolijk were the original ‘‘Team Fault Rocks’’ and contributed greatly to this work, as did conversations with Jeffrey Karson. Ken Livi, Scott Kuehner, Ron Sletten, David Joswiak, and Richard Stewart (*In Memoriam*) are thanked for access to laboratories and assistance. Chris Marone is thanked for convening a field forum. Jennifer Locke provided assistance with laboratory work. Reviews by Judith Chester, Ron Biegel, Laurel Goodwin, and Jay Ague greatly improved the manuscript. This work was supported by NSF-EAR 9417759 (to Darrel Cowan) and NSF-OCE 0222154 (to Jeffrey Karson). Partial support was received from the donors of the Petroleum Research Fund, administered by the American Chemical Society. Additional support was received from the Kraus Crystallographic Research Fund of the American Mineralogical Society.

References

Anthony, J.L., Marone, C., 2005. Influence of particle characteristics on granular friction. Journal of Geophysical Research 110, B08409, doi:10.1029/2004JB003399.

Ague, J.J., 2003. Fluid infiltration and transport of major, minor, and trace elements during regional metamorphism of carbonate rocks, Wepawaug schist, Connecticut, USA. American Journal of Science 303, 753–816.

Ague, J.J., Van Haren, J.L.M., 1996. Assessing metasomatic mass and volume changes using the Bootstrap, with application to deep hydrothermal alteration of marble. Economic Geology 91, 1169–1182.

An, L.J., Sammis, C.G., 1994. Particle size distribution of cataclastic fault materials from Southern California; a 3-D study. Pure and Applied Geophysics 143, 203–227.

Asmerom, Y., Snow, J.K., Holm, D.K., Jacobsen, S.B., Wernicke, B.P., Luz, D.R., 1990. Rapid uplift and crustal growth in extensional

environments: an isotopic study from the Death Valley region, California. Geology 18, 227–230.

Axen, G.J., 2004. Mechanics of low-angle normal faults. In: Karener, G.D., Taylor, B., Driscoll, N.W., Kohlstedt, D.L. (Eds.), Rheology and Deformation of the Lithosphere at Continental Margins. Columbia University Press, pp. 46–91.

Beeler, N.M., 2004. Review of the physical basis of laboratory-derived relations for brittle failure and their implications for earthquake occurrence and earthquake nucleation. Pure and Applied Geophysics 161, 18553–18576.

Blakely, R.J., Ponce, D.A., 2001. Map Showing Depth to Pre-Cenozoic Basement in the Death Valley Ground-Water Model Area, Nevada and California: U.S. Geological Survey Miscellaneous Field Studies Map MF-2381-E. U.S. Geological Survey, Denver, Colorado.

Byerlee, J., 1978. Friction of rocks. Pure and Applied Geophysics 116, 615–626.

Byrnes, S., 1989, A reconnaissance study of brittle deformation along frontal faults of the Black Mountains, Death Valley, California. M.Sc. thesis, University of New Orleans, 81 pp.

Chan, M.A., Parry, W.T., Bowman, J.R., 2000. Diagenetic hematite and manganese oxides and fault-related fluid flow in Jurassic sandstones, southeastern Utah. AAPG Bulletin 84, 1281–1310.

Chester, F.M., Chester, J.S., 1998. Ultracataclasite structure and friction processes of the Punchbowl fault, San Andreas System, California. Tectonophysics 295, 199–221.

Chester, F.M., Logan, J.M., 1987. Composite planar fabric of gouge from the Punchbowl fault, California. Journal of Structural Geology 9, 621–634.

Chester, F.M., Evans, J.P., Biegel, R.L., 1993. Internal structure and weakening mechanisms of the San Andreas fault. Journal of Geophysical Research 98, 771–786.

Chester, J.S., Chester, F.M., Kronenberg, A.K., 2005. Fracture surface energy of the Punchbowl fault, San Andreas system. Nature 437, 133–136.

Cho, H., Waters, M.A., Hogg, R., 1996. Investigation of grind limit in stirred-media milling. International Journal of Mineral Processing 44-45, 607–615.

Cladouhos, T.T., 1999a. Shape preferred orientations of survivor grains in fault gouge. Journal of Structural Geology 21, 419–436.

Cladouhos, T.T., 1999b. A kinematic model for deformation within brittle shear zones. Journal of Structural Geology 21, 437–448.

Collettini, C., Barchi, M.R., 2002. A low-angle normal fault in the Umbria region (Central Italy): a mechanical model for the related microseismicity. Tectonophysics 359, 97–115.

Cowan, D.S., 1999. Do faults preserve a record of seismic slip? A field geologist's opinion. Journal of Structural Geology 21, 995–1001.

Cowan, D.S., Cladouhos, T.T., Morgan, J., 2003. Structural geology and kinematic history of rocks formed along low-angle normal faults, Death Valley, California. Geological Society of America Bulletin 115, 1230–1248.

Drewes, H., 1963. Geology of the Funeral Peak Quadrangle, California, on the eastern flank of Death Valley. U.S. Geological Survey Professional Paper 413, 78.

Engelder, J.T., 1974. Cataclasis and the generation of fault gouge. Geological Society of America Bulletin 85, 1515–1522.

Evans, J.P., Chester, F.M., 1995. Fluid-rock interaction in faults of the San Andreas system; inferences from San Gabriel Fault rock geochemistry and microstructures. Journal of Geophysical Research 100, 13,007–13,020.

Faulkner, D.R., Rutter, E.H., 2001. Can the maintenance of overpressured fluids in large strike-slip fault zones explain their apparent weakness? Geology 29, 503–506.

Feng, X., Faiia, A.M., Gabriel, G., Aronson, J.L., Page, M.A., Chamberlain, C.P., 1999. Oxygen isotope studies of illite/smectite and clinoptilolite from Yucca Mountain; implications for paleohydrologic conditions. Earth and Planetary Science Letters 171, 95–106.

Garrels, R.M., Christ, C.L., 1965. Solutions, Minerals, and Equilibria. Freeman, Cooper & Co, San Francisco, CA, 449 pp.

Grant, J.A., 1986. The isocon diagram – a simple solution to Gresens' equation for metasomatic alteration. Economic Geology 81, 1976–1982.

Gresens, R.L., 1967. Composition-volume relationships of metasomatism. Chemical Geology 2, 47–65.

Hadizadeh, J., Johnson, W.K., 2003. Estimating local strain due to comminution in experimental cataclastic textures. Journal of Structural Geology 25, 1973–1979.

Hayman, N.W., 2003, Structure and petrology of gouge and breccia bearing shallow crustal shear zones of detachment faults in Death Valley, California. Ph.D. Dissertation, University of Washington, 176 pp.

Hayman, N.W., Knott, J.R., Cowan, D.S., Nemser, E., Sarna-Wojcicki, A., 2003. Quaternary low-angle slip on detachment faults in Death Valley, California. Geology 31, 343–346.

Hayman, N.W., Housen, B.A., Cladouhos, T.T., Livi, K., 2004. Magnetic and clast fabrics as measurements of grain-scale processes within the Death Valley shallow-crustal detachment faults. Journal of Geophysical Research 109, B05409, doi:10.1029/2003JB002902.

Helgeson, H.C., Brown, T.H., Leeper, R.H., 1979. Handbook of Theoretical Activity Diagrams Depicting Chemical Equilibria in Geologic Systems Involving an Aqueous Phase at One Atm and 0° to 300 °C. Freeman, Cooper & Co, San Francisco, CA, 253 pp.

Holm, Dokka, 1993. Interpretation and tectonic implications of cooling histories; an example from the Black Mountains, Death Valley extended terrane, California. Earth and Planetary Science Letters 116, 63–80.

Holm, D.K., Fleck, R.J., Lux, D.R., 1994. The Death Valley Turtlebacks reinterpreted as Miocene-Pliocene folds of a major detachment surface. Journal of Geology 102, 718–727.

Huang, W.L., Longo, J.M., Pevear, D.R., 1993. An experimentally derived kinetic model for smectite-to-illite conversion and its use as a geothermometer. Clays and Clay Minerals 41, 162–177.

Knott, J.R., Sarna-Wojcicki, A.M., Meyer, C.E., Tinsley III, J.C., Wells, S.G., Wan, E., 1999. Late Cenozoic stratigraphy and tephrochronology of the western Black Mountains piedmont, Death Valley, California:implications for the tectonic development of Death Valley. In: Wright, L.A., Troxel, B.W. (Eds.), Cenozoic Basins of the Death Valley Region. Geological Society of America Special Paper 333, 345–366.

Kopf, A., 2001. Permeability variation across an active low-angle detachment fault, western Woodlark Basin (ODP Leg 180), and its implication for fault activation. In: Holdsworth, R.E., Strachan, R.A., Magloughlin, J.F., Knipe, R.J. (Eds.), The Nature and Tectonic Significance of Fault Zone Weakening. Geol. Soc. London, Spec. Publications 186, 23–41.

Lister, G.S., Davis, G.A., 1989. The origin of metamorphic core complexes and detachment faults formed during tertiary continental extension in the northern Colorado River region, USA. Journal of Structural Geology 11, 65–94.

Losh, S., 1997. Stable isotope and modeling studies of fluid-rock interaction associated with the Snake Range and Mormon Peak detachment faults, Nevada. Geological Society of America Bulletin 109, 300–323.

Mair, K., Frye, K., Marone, C., 2002. Influence of grain characteristics on the friction of granular shear zones. Journal of Geophysical Research 107, 2219, doi:10.1029/2001JB000516.

Manatschal, G., Marquer, D., Fruh-Green, G.L., 2000. Channelized fluid flow and mass transfer along a rift-related detachment fault (Eastern Alps, southeast Switzerland). Geological Society of America Bulletin 112, 2–33.

Marone, C., 1998. Laboratory-derived friction laws and their applications to seismic faulting. Annual Review of Earth and Planetary Science 26, 643–696.

Means, W.D., 1995. Shear zones and rock history. Tectonophysics 247, 157–164.

Miller, M.G., 1992. Brittle faulting induced by ductile deformation of a rheologically stratified rock sequence, Badwater Turtleback, Death Valley, California. Geological Society of America Bulletin 104, 1376–1385.

Miller, M.G., 1996. Ductility in fault gouge from a normal fault system, Death Valley, California: a mechanism for fault-zone strengthening and relevance to paleoseismicity. Geology 24, 603–606.

Moore, D.M., Reynolds, R.C., 1997. X-ray Diffraction and the Identification and Analysis of Clay Minerals. Oxford University Press, US, 400 pp.

Morgan, J.K., 1999. Numerical simulations of granular shear zones using the distinct element method 2. Effects of particle size distribution and interparticle friction on mechanical behavior. Journal of Geophysical Research 104, 2721–2732.

Morgan, J.K., Boettcher, M.S., 1999. Numerical simulations of granular shear zones using the distinct element method; 1, Shear zone kinematics and the micromechanics of localization. Journal of Geophysical Research 104, 2703–2719.

Morgan, J.K., Cladouhos, T.T., Scharer, K.M., Cowan, D.S., Vrolijk, P.J., 1996. Fractal particle size distributions in Death Valley fault zones; controls on mechanics and kinematics of fault rocks. Eos, Transactions, American Geophysical Union 77, 717–718.

Morrison, J., Anderson, J.L., 1998. Footwall refrigeration along a detachment fault: Implications for the thermal evolution of core complexes. Science 279, 63–66.

Numelin, T., Marone, C., Kirby, E., 2004. Fault gouge mineralogy as a driver for variable frictional response in a low-angle normal fault setting. Geological Society of America. Abstracts with Programs 36, 548.

Pavlis, T.L., Serpa, L.F., Keener, C., 1993. Role of seismogenic processes in fault-rock development; an example from Death Valley, California. Geology 21, 267–270.

Rawling, G.C., Goodwin, L.B., 2003. Cataclasis and particulate flow in faulted, poorly lithified sediments. Journal of Structural Geology 25, 317–331.

Rice, J.R., 1992. Fault stress states, pore pressure distributions, and the weakness of the San Andreas fault. In: Evans, B., Wong, T.-F. (Eds.), Fault Mechanics and Transport Properties of Rocks. Academic, San Diego, CA, pp. 475–503.

Saffer, D.M., Marone, C., 2003. Comparison of smectite- and illite-rich gouge frictional properties: application to the updip limit of the seismogenic zone along subduction megathrusts. Earth and Planetary Science Letters 215, 219–235.

Sammis, C.G., King, G., Biegel, R., 1987. The kinematics of gouge deformation. Pure and Applied Geophysics 125, 777–812.

Sass, J.H., Lachenbruch, A.H., Galanis Jr., S.P., Morgan, P., Priest, S.S., Moses Jr., T.H., Munroe, R.J., 1994. Thermal regime of the southern Basin and Range Province; 1, Heat flow data from Arizona and the Mojave Desert of California and Nevada. Journal of Geophysical Research 99, 22,093–22,119.

Savin, S.M., Lee, M., 1988, Isotopic studies of phyllosilicates. In: Bailey, S.W. (Ed.), Hydrous Phyllosilicates. Mineralogical Society of America, Reviews in Mineralogy vol. 19, pp. 189–223.

Sibson, R.H., 1977. Fault rocks and fault mechanisms. Journal of the Geological Society of London 133, 191–213.

Sperazza, M., Moore, J.N., Hendrix, M.S., 2004. High-resolution particle size analysis of naturally occurring very fine-grained sediment through laser diffractometry. Journal of Sedimentary Research 74, 736–743.

Storti, F., Billi, A., Alvini, F., 2003. Particle size distributions in natural carbonate fault rocks: insights for non-self-similar cataclasis. Earth and Planetary Science Letters 206, 173–186.

Twiss, R.J., Moore, E.M., 1992. Structural Geology. Freeman Press, 532 pp.

Vrolijk, P.J., Cladouhos, T.T., Cowan, D.S., Morgan, J., 1997. Importance of alteration reactions for the Death Valley fault zone. Abstracts with Programs. Geological Society of America 29, 258.

Wilson, B., Dewers, T., Reches, Z., Brune, J., 2005. Particle size and energetics of gouge from earthquake rupture zones. Nature 434, 749–752.

Wright, L.A., Troxel, B.W., 1984. Geology of the northern half of the Confidence Hills 15-min Quadrangle, Death Valley region, eastern California; the area of the Amargosa chaos. Map Sheet 34. California Division of Mines and Geology, 34.

Wright, L.A., Otton, J.K., Troxel, B.W., 1974. Turtleback surfaces of Death Valley viewed as phenomena of extensional tectonics. Geology 2, 53–54.

Wright, L.A., Thompson, R.A., Troxel, B.W., Pavlis, T.L., DeWitt, E.H., Otton, J.K., Ellis, M.A., Miller, M., Serpa, L.F., 1991. Cenezoic magmatic and tectonic evolution of the east-central Death Valley region, California. In: Walawender, M.J., Hanan, B.B. (Eds.), Geological Excursions in Southern California and Mexico. Guidebook 1991 Annual Meeting Geological Society of America, pp. 93–127.

Yonkee, W.A., Parry, W.T., Bruhn, R.L., 2003. Relations between progressive deformation and fluid-rock interaction during shear-zone growth in a basement-cored thrust sheet, Sevier orogenic belt, Utah. American Journal of Science 303, 1–59.